JOURNAL OF THE AMERICAN CHEMICAL SOCIETY

Article

pubs.acs.org/JACS

# Reversible Switching from Antiferro- to Ferromagnetic Behavior by Solvent-Mediated, Thermally-Induced Phase Transitions in a Trimorphic MOF-Based Magnetic Sponge System

Mario Wriedt,[†] Andrey A. Yakovenko,[†] Gregory J. Halder,[‡] Andrey V. Prosvirin,[†] Kim R. Dunbar,[†] and Hong-Cai Zhou*,[†]

[†]Department of Chemistry, Texas A&M University, 3255 TAMU College Station, Texas 77843-3255, United States
[‡]X-ray Science Division, Advanced Photon Source, Argonne National Laboratory, 9700 South Cass Ave, Illinois 60439, United States

*Supporting Information*

**ABSTRACT:** Hydrothermal reactions of copper(II) acetate, tetrazolate-5-carboxylate (tzc), and the neutral N-donor spacer ligand 1,3-di(4-pyridyl)propane (dpp) lead in a single reaction vial to the simultaneous formation of three different single-crystalline solvates $[Cu(tzc)(dpp)]_n{\cdot}0.5C_6H_{14}{\cdot}0.5H_2O$ (**1**), $[Cu(tzc)(dpp)]_n{\cdot}4.5H_2O$ (**2**), and $[Cu(tzc)(dpp)]_n{\cdot}1.25C_6H_{14}$ (**3**). All three structures were characterized by single crystal X-ray diffraction. None of these solvates can be prepared as phase-pure bulk materials, but reaction conditions similar to those used for single crystal synthesis yield a phase-pure polycrystalline bulk material of an additional forth solvate phase $[Cu(tzc)(dpp)]_n{\cdot}2H_2O$ (**4**). Investigations of its thermal properties by *in situ* temperature-dependent synchrotron-based powder diffraction experiments have shown interesting phase transitions upon heating in a helium stream. Initially, the precursor dihydrate **4** transforms to an anhydrous phase $[Cu(tzc)(dpp)]_n$ (**6I**) *via* the intermediate monohydrate phase $[Cu(tzc)(dpp)]_n{\cdot}H_2O$ (**5**). Upon further heating, phase **6I** transforms to a new anhydrous polymorph **6II**, which transforms upon cooling to a further new phase **6III**. Thermogravimetric measurements performed in tandem with differential scanning calorimetry as well as infrared spectroscopic investigations are in agreement with these findings. The de/resolvation behavior is accompanied by a dramatic change in their magnetic properties: The dihydrate phase shows antiferromagnetic exchange interactions, whereas ferromagnetic properties are observed for the trimorphic anhydrate system. This magnetic sponge-like behavior can be reversibly cycled upon de/resolvation of the material.

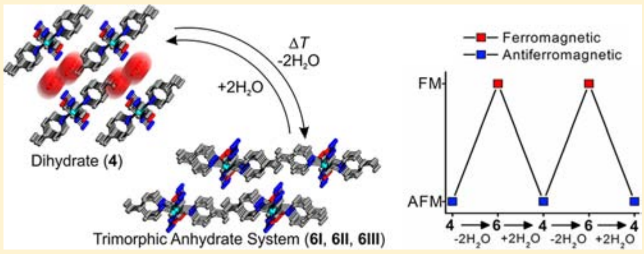

## ■ INTRODUCTION

Solid-state materials with two or more different physical properties have recently attracted intense interest, because such multifunctional materials offer the possible synergism of different functions and therefore new potential applications.[1] In this context, hybrid metal–organic frameworks (MOFs) are promising candidates for such materials because they can exhibit a wide range of potentially interdependent properties that are influenced by both the inorganic and organic components.[2]

Thus far, crystal engineering has led to the systematic design of open-framework structures whose structures as well as pore sizes and functionalities depend on the size and nature of the organic ligands.[3] Incorporation of paramagnetic transition metal ions into these frameworks opens up the possibility of obtaining porous materials with well-defined magnetic properties. Consequently, the search for magnetic open-framework structures has become an important challenge due to their potential applications in the development of low-density magnetic materials, magnetic sensors, and intelligent or multifunctional materials.[4]

Magnetic properties, such as ferromagnetism and antiferromagnetism, are derived from the cooperative exchange interactions between the paramagnetic metal cations through superexchange pathways of diamagnetic entities. Therefore, their magnetic behaviors depend on the intrinsic nature of both the metal and the organic ligand as well as the particular topology adopted by the metal–ligand coordination interaction. As a result, in pursuing the magnetism of MOFs, the ligand design is crucial both to organize the paramagnetic metal ions in a desired topology and to efficiently transmit magnetic exchange interactions between the metal ions in a controlled manner.

One of the most exciting findings in this field is that some MOFs can have flexible or dynamic structures,[5] which are inherently related to the flexibility of the metal–ligand coordination, the organic ligands, and/or noncovalent interactions. Such behavior is extremely useful in the preparation of sophisticated functional materials with tunable or switching physical properties. This is especially valid for magnetic materials because their properties are exquisitely sensitive to small structural changes and can also change dramatically as a function of external parameters such as temperature or pressure. In this context, we note that structural changes can also be induced by intercalation,

**Received:** December 26, 2012
**Published:** February 15, 2013

deintercalation, and/or even exchange of guest molecules. In this rein, flexible MOFs have attracted considerable attention in recent years, with fascinating magnetic properties being observed including guest-modulated magnetic ordering,[6] guest-sensitive spin crossover,[7] and guest-induced switching between different magnetic states.[8] The modulation or switching of magnetic properties in these systems is usually induced by the removal, reabsorption, or exchange of guest molecules, which can be connected to the metal cations or the organic linker ligands or completely independent of the host framework structure.

With the above considerations in mind, we prepared a series of new magnetic MOF materials based on the anionic ligand tetrazolate-5-carboxylate ($tzc^{2-}$) and different neutral N-donor spacer ligands namely materials of basic formulas $[Cu(tzc)(pyrazine)]_n$ and $[Cu(tzc)(pyrimidine)(H_2O)]_n$.[9] In this context, tzc has been confirmed to be an excellent bridging ligand for the formation of coordination compounds exhibiting great structural diversity and interesting magnetic properties. With the carboxylate and tetrazolate group linked directly, this ligand can exhibit a large number of potential coordination modes due to its abundance of N- and O-donor sites and their unique arrangement in space. Moreover, as a small and conjugated ligand, it offers short potential magnetic superexchange pathways which lead to it being an excellent magnetic coupling mediator between paramagnetic metal centers.[9,10] In the course of our systematic investigations of the reaction between Cu(tzc) units and the N-donor ligand 1,3-di(4-pyridyl)propane (dpp) we first discovered $[Cu(tzc)(dpp)_{0.5}]_n$, a porous MOF material which can selectively capture $CO_2$ molecules by an elastic single-molecule trapping mechanism.[11] In the current work we have extended this chemistry to the synthesis and characterization of a series of eight new materials with the core composition $[Cu(tzc)(dpp)]_n$. These compounds show reversible solvent-mediated and thermally-induced phase transitions accompanied by dramatic changes in their magnetic properties. Herein we report the interesting structure−property relationships investigated by temperature-dependent synchrotron-based powder diffraction (SPD) experiments and magnetic measurements. In addition, the thermodynamic relationships between different polymorphic modifications are discussed in detail.

## ■ RESULTS AND DISCUSSION

**Synthesis and Crystal Structures of $[Cu(tzc)(dpp)]_n$ Solvates (1−4).** Hydrothermal treatment of Cu(tzc) with dpp (ratio 1:1) in a single reaction vial leads to a heterogeneous mixture of three different single-crystalline solvates $[Cu(tzc)(dpp)]_n \cdot 0.5C_6H_{14} \cdot 0.5H_2O$ (**1**), $[Cu(tzc)(dpp)]_n \cdot 4.5H_2O$ (**2**), and $[Cu(tzc)(dpp)]_n \cdot 1.25\ C_6H_{14}$ (**3**). Their structures were determined and refined by X-ray single crystal structure analysis (see Experimental section). Solvate **1** crystallizes in the triclinic space group $P\bar{1}$ (Table 4). The asymmetric unit consists of two Cu(II) cations located on a center of inversion (occupancy 1/2), one dpp and tzc ligand as well as one water and one hexane molecule in crystallographically independent general positions (Figure S1). Solvates **2** and **3** crystallize in the monoclinic space group $C2/c$ (Table 4). The asymmetric unit of both compounds consist of two Cu(II) cations, one dpp and tzc ligand, all located in crystallographically independent general positions (Figures S2 and S3). Due to severe disorder of the solvent molecules in **2** and **3**, their location could not be determined (see Experimental section). All solvates **1**−**3** have the same Cu(tzc)/dpp composition and differ only in their content of noncoordinating solvent molecules leading to the same structural topology. In their crystal structure each Cu(II) cation is ligated by two symmetry-related tzc ligands and two symmetry-related dpp ligands in an octahedral geometry, while adjacent Cu(II) cations are each bridged by one tzc and one dpp ligand forming 1D chains (Figure 1). Each tzc ligand bridges two Cu(II) cations through both carboxylate oxygen atoms and through two opposite nitrogen atoms of the tetrazolate unit to give a $\mu_2$-N1, O1:N4, O2 bridging mode, whereas each dpp ligand connects two Cu(II) cations in a $\mu_2$-N11:N12 bridging mode (Figure 1). Further structural information of solvates **1**−**3** is provided in the Supporting Information (SI). The structural arrangement, especially the Cu−tzc−Cu bridge, provides a promising pathway for interesting magnetic exchange interactions. The resulting $CuN_4O_2$ octahedron exhibits bond distances and angles in the normal range for similar compounds.

Similar hydrothermal reaction conditions as used for single crystal synthesis (see Experimental section) yield a phase-pure polycrystalline bulk material of a new solvate phase $[Cu(tzc)(dpp)]_n \cdot 2H_2O$ (**4**) showing a very similar X-ray powder diffraction pattern as simulated for compound **1** (Figure S4). Starting with this knowledge we succeeded in solving and refining the structure of the dihydrate **4** from SPD data (see Experimental section). This compound crystallizes in the triclinic space group $P\bar{1}$ (Table 5) and has a structure containing $[Cu(tzc)(dpp)]_n$ chains similar to that found in compound **1** (Figure 1). The chains elongate along the crystallographic *c*-axis and are packed in the direction of the *b*-axis with noncoordinating water molecules occupying the interchain voids (Figure 11A). Intrachain metal−metal separations through the tzc/dpp ligand are found to be 5.6482(4) Å, whereas the shortest interchain separation of two adjacent Cu(II) cations is 9.0102(8) Å (Table 1).

**Thermal Properties of $[Cu(tzc)(dpp)]_n \cdot 2H_2O$ (4).** On heating the dihydrate $[Cu(tzc)(dpp)]_n \cdot 2H_2O$ (**4**), three mass loss steps are observed in the thermogravimetric (TG) curve (Figure 3, black curve). The first two TG steps are not well resolved, whereas the third TG step is clearly separated. Heating rate-dependent TG measurements to further improve the resolution were unsuccessful. From the mass spectrometry (MS) trend scan curve of the TG exhaust gas, it is verified that only water ($m/z$ = 18) is lost in the first two mass steps as well as dpp ($m/z$ = 198) and nitrogen ($m/z$ = 28, decomposition product of tzc) in the third step (Figure 3, colored curves). The experimental mass loss of $\Delta m_{exp}$(first + second step) = 8.9% is in excellent agreement with that calculated for the release of two water molecules [$\Delta m_{calc}$(water) = 8.8%], which is equal to one water molecule per step. On the basis of the experimental mass losses, it can be assumed that in the second step an anhydrous compound $[Cu(tzc)(dpp)]_n$ (**6I**) is formed *via* the formation of a monohydrate $[Cu(tzc)(dpp)]_n \cdot H_2O$ (**5**) before **6I** starts decomposing at ∼190 °C. The DSC curve is in agreement with this TG evaluation: The water removal steps are accompanied by a smooth broad endothermic event and the third step by an exothermic event corresponding to the anhydrate's decomposition (Figure 4). Moreover, the DSC curve shows a further endothermic event at around 129 °C. Based on this observation it can be assumed that the anhydrate **6I** transforms into a new polymorphic modification **6II** before decomposition of the material. The energy consumption for this phase transition was estimated to be $\Delta H = -17.7\ kJ \cdot mol^{-1}$.

**Investigations of Materials Formed upon Phase Transitions.** In order to verify the nature of the intermediate monohydrate **5** and anhydrate modifications **6I** and **6II** formed, various synthetic routes were tested to isolate these materials.

**Table 1. Selected Bond Lengths [Å] and Angles [°] Refer to the Labelling Scheme in Figure 2**

| compound | 4 | 5 | 6I | 6II | 6III |
|---|---|---|---|---|---|
| Cu1−$N_{tzc1}$ | 2.1143(1) | 2.0079(1) | 2.72(2) | 2.260(3) | 2.0398(1) |
| Cu2−$N_{tzc1}$ | 2.0193(2) | 2.3205(1) | 2.16(2) | – | 2.4967(1) |
| Cu1−$N_{dpp1}$ | 2.0585(2) | 1.9660(2) | 2.00(2) | 2.107(3) | 2.0865(1) |
| Cu2−$N_{dpp1}$ | 2.0149(2) | 1.9265(1) | 2.38(2) | – | 2.0434(1) |
| Cu1−$O_{tzc1}$ | 2.4565(2) | 2.3130(1) | 1.92(2) | 2.266(3) | 2.4217(1) |
| Cu2−$O_{tzc1}$ | 2.4387(1) | 2.2943(2) | 2.67(2) | – | 2.0663(1) |
| Cu1−$N_{tzc}$−$C_{tzc}$ | 115.362(3) | 106.933(4) | 106.1(5) | 105.87(3) | 110.455(1) |
| Cu2−$N_{tzc}$−$C_{tzc}$ | 110.790(3) | 111.374(4) | 113.7(6) | – | 99.944(1) |
| $\alpha_1$ | 85.965(1) | 87.890(1) | 80.2(1) | 82.54(1) | 85.215(1) |
| $\alpha_2$ | 84.861(1) | 83.829(1) | 81.3(1) | – | 76.716(1) |
| $\beta_1$ | 168.208(1) | 166.288(1) | 163.6(1) | 163.91(1) | 168.277(1) |
| $\beta_2$ | 171.298(1) | 170.822(1) | 170.6(1) | – | 159.841(1) |
| Cu···Cu intrachain[a] | 5.6482(4) | 5.6575(3) | 5.47(3) | 5.613(1) | 5.5880(2) |
| Cu···Cu interchain[a] | 9.0102(8) | 8.8876(6) | 8.30(3) | 8.647(1) | 8.6065(2) |

[a] Shortest Cu···Cu interactions.

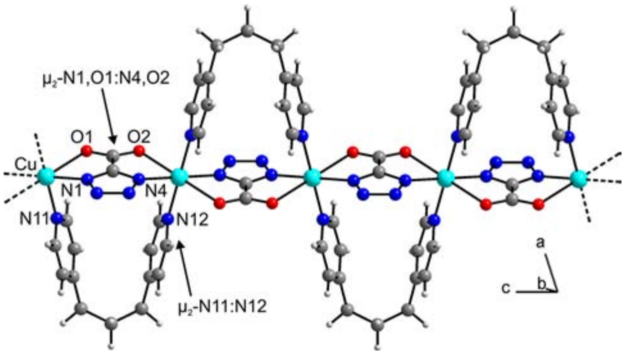

**Figure 1.** Crystal structure of $[Cu(tzc)(dpp)]_n \cdot 2H_2O$ (**4**) with view onto a single 1D $[Cu(tzc)(dpp)]_n$ chain as representative structural topology of compounds **1**, **2**, and **6I–III**. The structure of **3** is shown in Figure S3. The solvent molecules are omitted for the sake of clarity.

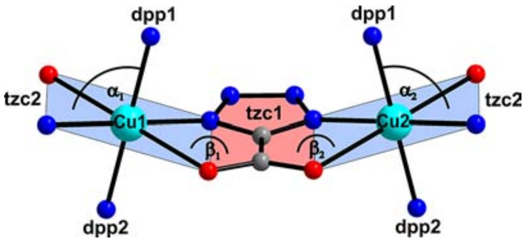

**Figure 2.** Description of the Cu(II) coordination environment of the compounds presented in this manuscript. $\beta$ denotes the dihedral angle between the tzc and $Cu(N_{tzc})_2(O_{tzc})_2$ plane, and $\alpha$ denotes the angle between the latter plane and the line formed by two opposite $N_{dpp}$ atoms.

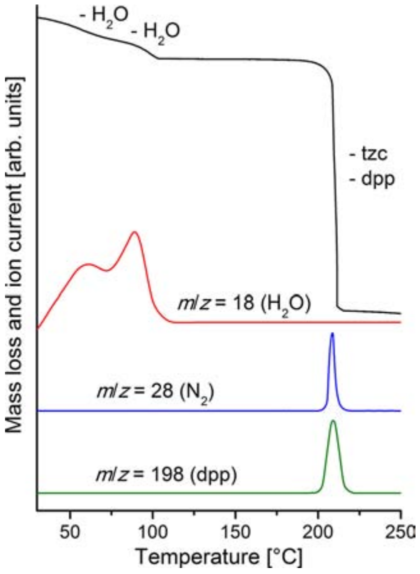

**Figure 3.** TG and MS trend scan curves for compound **4**. Heating rate = 3 °C·min$^{-1}$; $m/z$ = 18 (water), 28 ($N_2$, decomposition product of tzc), and 198 (dpp).

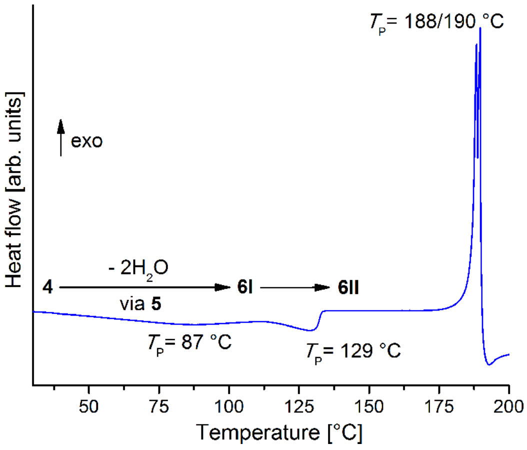

**Figure 4.** DSC curve for compound **4**. Heating rate = 3 °C·min$^{-1}$; given are the peak temperatures $T_P$ [°C].

Heating precursor **4** to 100 and 150 °C, respectively, followed by a 30 min isothermal step at each temperature was found to be suitable conditions to synthesize modifications **6I** and **6II** in gram quantities. The phases obtained were investigated by elemental analysis, infrared spectroscopy (Figure 7), SPD experiments (Figures 5B and 6), and magnetic measurements (Figures 12 and 13). Finally, *in situ* SPD experiments were performed to get full insight in the structural changes upon phase transitions (Figures 5A and 8).

All attempts to isolate the monohydrate **5** in the thermal decomposition reaction of the dihydrate **4** were unsuccessful. Compound **5**, however, was observed as an intermediate in an *in situ* SPD experiment by purging helium through **4** (Figure 5A). Upon exposure to regular air, this process is reversible, and the

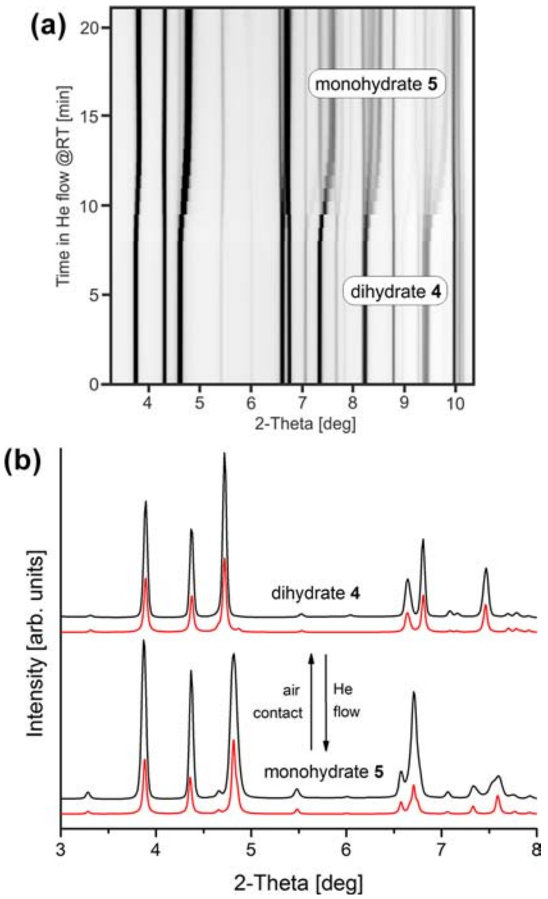

**Figure 5.** *In situ* SPD pattern: Upon purging helium through the dihydrate **4**, a phase transition is observed leading to the intermediate monohydrate **5** (A). The extracted experimental SPD patterns (black) match the ones simulated from structural data (red), supporting the existence of pure phases (B).

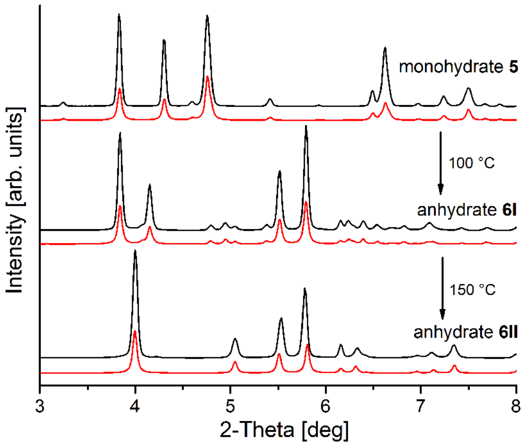

**Figure 6.** Experimental (black) and simulated (red) XRPD patterns of the monohydrate **5** (top) and the intermediate anhydrate phases **6I** (middle) and **6II** (bottom).

monohydrate **5** transforms back to the dihydrate **4**. The SPD data can be indexed to a triclinic unit cell with parameters similar to those found for **4** (Table 5) and the crystal structure was solved and refined based on this data (see Experimental section). The structure and packing of **5** are analogous to that of **4**; each copper(II) cation is coordinated with two bridging dpp and tzc ligands in an octahedral geometry forming 1D chains, which are packed along the *b*-axis (Figure 11, compare A with B). The smallest interchain separation of two adjacent Cu(II) cations has decreased from 9.0102(8) Å in **4** to 8.8876(6) Å in **5** due to the loss of one noncoordinating interchain water molecule (Table 1).

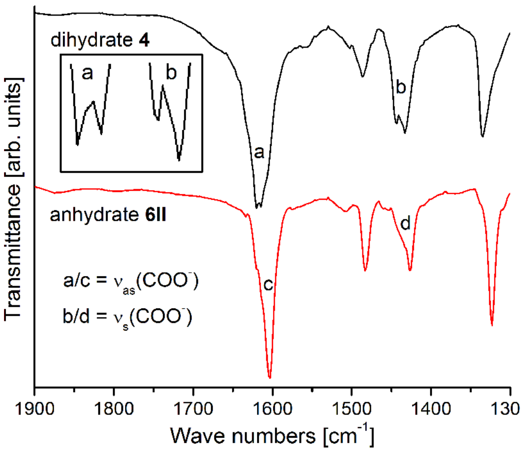

**Figure 7.** IR spectra of the dihydrate **4** (black) and the anhydrate phase **6II** (red) labeled with the asymmetric $\nu_{as}$ (~1600 cm$^{-1}$, a/c) and symmetric $\nu_s$ (~1400 cm$^{-1}$, b/d) carboxylate vibration modes. The inset shows an expanded view of the (a) and (b) regions in the IR spectra of **4**.

Investigations of freshly synthesized **6I** revealed the same elemental composition, IR spectra, and XRPD pattern as found for the dihydrate **4**. Thus, it can be assumed that the anhydrate reversibly reverts back to the dihydrate **4** upon contact with atmospheric moisture. Compound **6I**, however, can be handled under inert gas conditions. This process was monitored by *ex situ* SPD experiments (Figure 5B). The SPD pattern of the intermediate phase **6I** was indexed to a triclinic unit cell (Table 5), and the crystal structure was solved and refined based on this data (see Experimental section). In general the crystal structure is similar to **4** with each Cu(II) cation being coordinated to bridging dpp and tzc ligands in an octahedral geometry that form 1D chains along the crystallographic *a*-axis (*c*-axis in **4**). In comparison to **4**, the chain packing has changed dramatically due to the removal of the noncoordinating interchain water molecules (Figure 11, compare A and B with C). The smallest interchain separation of two adjacent Cu(II) cations and the intrachain metal—metal separations through the tzc/dpp ligand have decreased from 9.0102(8) and 5.6482(4) Å in **4** to be 8.30(3) and 5.47(3) Å in **6I** (Table 1).

Elemental analysis of phase **6II** leads to an elemental composition as expected for an anhydrate of composition $[Cu(tzc)(dpp)]_n$ (see Experimental section). IR spectroscopic investigations were performed to gain insight into the structural changes accompanying the phase transition (Figure 7). The magnitude of the separation between the asymmetric ($\nu_{as}$, ~1600 cm$^{-1}$) and symmetric ($\nu_s$, ~1400 cm$^{-1}$) carboxylate stretches ($\Delta = \nu_{as} - \nu_s$) is often used as a spectroscopic criterion to determine the mode of the carboxylate binding.[12] Values of $\nu_{as}$ = 1604 cm$^{-1}$ (1620/1614 cm$^{-1}$ for **4**) and $\nu_s$ = 1426 cm$^{-1}$ (1444/1433 cm$^{-1}$ for **4**) were found for a value of $\Delta$ = 178 cm$^{-1}$ (176/181 cm$^{-1}$ for **4**), which is typical for *anti*—*anti* bridging carboxylate anions.[12] These findings comply with the $\mu_2$-N1, O1:N4, O2 bridging mode of the tzc ligand in the crystal structure of **4** obtained from X-ray powder data (described above). Because of comparable $\Delta$ values of **4** and **6II**, it can be

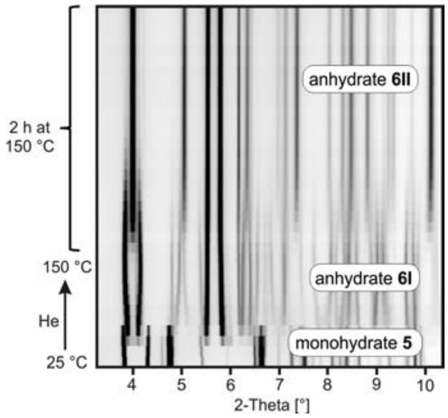

**Figure 8.** *In situ* SPD pattern: Upon heating in a helium flow, the monohydrate **5** transforms *via* the intermediate anhydrate **6I** into the anhydrate **6II**. Originally, this experiment was performed with the dihydrate **4** as the precursor. It was found that **4** transformed in the applied He flow into the monohydrate **5** before the SPD data collection was started.

assumed that the overall structural topology is retained upon phase transition. The most distinguished difference in their IR spectra, however, splits in the $\nu_{as}$ and $\nu_s$ bands in **4** (Figure 7, top), which are attributed to two crystallographically independent Cu–$O_{carboxylate}$ bonds consistent with the triclinic symmetry, whereas **6II** exhibits single $\nu_{as}$ and $\nu_s$ bands (Figure 7, bottom) attributed to energetically equal Cu–$O_{carboxylate}$ bonds. These data indicate that the phase transition leads to a higher symmetry for **6II**.

Based on these findings the SPD pattern of **6II** was indexed to a higher symmetry orthorhombic unit cell (Table 5). Form **6II** was found to crystallize in the space group *Pnma*, and its structure was determined based on the SPD data (see Experimental section). In this phase, the coordination environment of the Cu(II) cations remains unchanged with 1D chains being formed by $\mu_2$-dpp/tzc bridged Cu(II) cations. Due to the symmetry change, however, these chains are elongated **6II** along the crystallographic *b*-axis (*a*-axis in **6I**), which are packed along the crystallographic *c*-axis (*b*-axis in **6I**) (Figure 11, compare C with D). Furthermore, this phase transition is accompanied by a significant decrease of the cell volume from 1710.4 Å$^3$ in **6I** to 1676.4 Å$^3$ in **6II**. This implies that **6I** has interchain voids as compared to **6II**, which might explain the water sensitivity of **6I** and the water stability of **6II**. An alternate explanation is that **6II** is the thermodynamically stable form over the investigated temperature range, which would be expected to be more water inert than the metastable form **6I** (see Thermodynamic Relations of the Trimorphic System section). The shortest interchain separation of two adjacent Cu(II) cations increases to 8.6471(2) Å (8.30(3) Å in **6I**), and the intrachain metal–metal separations through the tzc/dpp ligand are 5.6126(1) Å (5.47(3) Å in **6I**) (Table 1).

*In situ* temperature-dependent SPD experiments are in agreement with the above-mentioned *ex situ* investigations: Upon heating, the monohydrate **5** transforms *via* the intermediate anhydrate **6I** into the anhydrate **6II**, no indication for the formation of additional intermediate phases can be found (Figure 8).

In the course of the aforementioned structural investigation, SPD data were collected at various temperatures to gain deeper insight into the dimorphic nature of the phases (**6I** and **6II**). In this context, the powder patterns of **6II** collected at 100 K exhibit significant differences, e.g., the 111 reflection at 295 K (~3.5° 2-$\theta$) splits into 111 and 11−1 reflections (Figure 9).

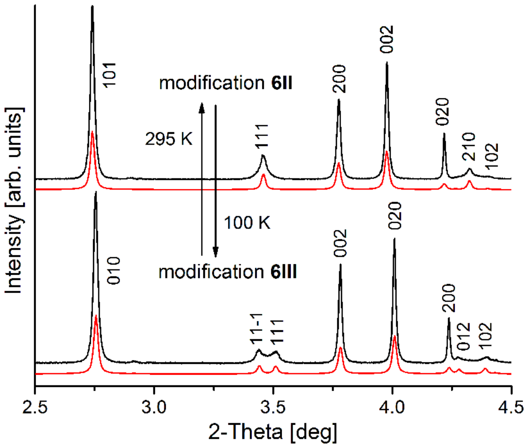

**Figure 9.** Experimental (black) and simulated (red) SPD patterns of the polymorphic anhydrate modifications **6II** (top, collected at 295 K) and **6III** (bottom, collected at 100 K).

The powder pattern collected at 100 K was indexed to a monoclinic unit cell and corresponds to the space group $P2_1/c$ (Table 5), which supports the existence of an additional polymorphic anhydrous modification **6III**. The crystal structure of **6III** was determined and found to retain the overall structure topology (Figure 11, compare D with E) with only small changes in bond lengths and angles as compared to **6II**. The most pronounced changes with the phase transitions are that the interchain separation of two adjacent Cu(II) cations decreases from 9.0102(8) Å in **4** to 8.6065(2) Å in **6III** (Table 1).

### Thermodynamic Relations of the Trimorphic System.

Polymorphs are categorized into two types, monotropes and enantiotropes, depending upon their stability with respect to the range of temperature and pressure. For an enantiotropic system, plots of their temperature-dependent free energy $G(T)$ show a crossing, which is not the case if the thermodynamic relationship is one of monotropism.[13]

Upon heating, the triclinic phase **6I** transforms around $T_t$(**6I** → **6II**) = 129 °C into the orthorhombic phase **6II**. Thus, **6I** is thermodynamically stable at lower temperatures, where **6II** is metastable. At higher temperatures the situation is reversed, namely **6I** becomes metastable, and **6II** is stable. Because of potential hysteresis, the transition temperatures determined by our DSC investigations might be shifted to higher temperatures and do not correspond to the true thermodynamic transition temperature. Although this transition is not reversible within the time scale of the experiment, the abrupt endothermic polymorphic phase transition (Figure 4) from phase **6I** to **6II** clearly indicates that both forms are related by enantiotropism as schematically indicated by their crossing temperature-dependent free energy curves in Figure 10, left. From DSC measurements, the enthalpy of transformation was estimated to be $\Delta H_t$(**6I** → **6II**) = −17.7 kJ·mol$^{-1}$. Even if the structures of **6I** and **6II** are very similar, the reaction pathway presumably proceeds *via* nucleation and growth of a new phase (polymorphic first-order reconstructive transition).

Upon cooling **6II**, the monoclinic phase **6III** can be observed at 100 K. Thus, **6III** is thermodynamically stable at lower temperatures, where **6II** is metastable. This transformation is a smooth process as indicated by *in situ* SPD experiments (Figure S5). Upon warming, the phase change is reversible, which indicates that modifications **6II** and **6III** are enantiotropically related (Figure 10, right). According to additional DSC and SPD experiments no direct

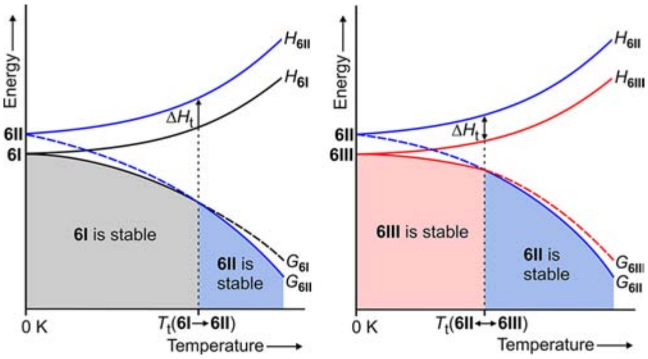

**Figure 10.** Qualitative energy-temperature diagram for the enantiotropically related polymorphs **6I**/**6II** (left) and **6II**/**6III** (right). Modification **6I** transforms upon heating in form **6II** (left), which transforms upon cooling in form **6III** (right) with $T_t$(**6I** → **6II**) > $T_t$(**6II** ↔ **6III**). The latter process is reversible ($G$ = free energy, $H$ = enthalpy, $\Delta H_t$ = enthalpy of transformation, $T_t$ = transition temperature).

transition between the modifications **6I** and **6III** can be observed. However, based on the present data, conclusions about the energetic relation of modifications **6I** and **6III** cannot be drawn.

**Magneto–Structural Investigations.** The superexchange capacity of the tetrazolate unit can lead to interesting magnetic properties as frequently discovered for tzc-containing materials.[9,10] As shown in one of our previous studies, tzc-bridged copper(II) centers in a $\mu_2$-N1, O1:N4, O2 bridging mode (as found in all the new compounds presented herein) exhibit antiferromagnetic coupling.[9] As part of our continuing systematic investigation of magneto–structural correlations in this class of compounds, we investigated the magnetic properties of compounds **4**, **6I** and **6II** by measuring the temperature dependence of the dc susceptibility and their isothermal magnetization (for details see Experimental section). In this context it must be noted that the low-temperature magnetic properties of **6II** cannot be determined because it transforms upon cooling in **6III**. Therefore, **6II** is referred in the following section as **6II**/**III** (see Figure 11).

[Cu(tzc)(dpp)]$_n$·2H$_2$O (**4**): The $\chi_M T$ plots of all herein presented compounds are shown in Figure 12. Temperature-independent $\chi_M T$ values for the dihydrate **4** were recorded in the range 300–100 K with a value of 0.42 emu·K·mol$^{-1}$ at 300 K, corresponding to the effective magnetic moment of $\mu_{\mathrm{eff}}$ = 1.87 $\mu_B$, which is slightly higher than the expected value for a spin-only case ($\mu_{\mathrm{eff}}$ = 1.73 $\mu_B$, $S$ = 1/2, $g$ = 2.0) and which is not unusual given spin–orbit coupling, zero-field splitting, and $g$ values >2.0 (Table 2). Upon further cooling, decreasing $\chi_M T$ values are observed beginning at ~100 K, a signature of antiferromagnetic exchange interactions between Cu(II) centers. The $\chi_M^{-1}$ vs $T$ curve is essentially linear and follows a Curie–Weiss law (Figure S6) with a Curie constant of $C$ = 0.44 cm$^3$·K·mol$^{-1}$ and a negative Weiss constant $\theta$ = −4.0 K consistent with the antiferromagnetic behavior (Table 2).

In the crystal structure of **4** the tzc ligands are nearly symmetrically aligned between the Cu(II) centers to yield very similar pairs of Cu–N$_{\mathrm{tzc}}$/O$_{\mathrm{tzc}}$ bond distances (Figure 14). The Cu(II) $d_{x^2-y^2}$ magnetic orbitals are directed toward the N$_{\mathrm{tzc}}$ nitrogen atoms, which leads to the imidazolyl exchange pathway being the one responsible for the magnetic coupling. The magnetic exchange interactions through the carboxylato part of the tzc ligand are considered to be negligible because the O$_{\mathrm{tzc}}$ atoms are weakly coordinated in axial positions with long O$_{\mathrm{tzc}}$–Cu distances of ~2.5 Å. Interchain interactions can be excluded due to the large interchain separation of the Cu(II) centers. Taking these considerations into account, the magnetic data were fitted by using a Heisenberg exchange model by Hatfield et al. for $S$ = 1/2 systems.[14] The Hamiltonian is written as

$$H = -2J \sum_{i=1}^{n/2} [\hat{S}_{2i}\cdot\hat{S}_{2i-1} + \alpha\hat{S}_{2i}\cdot\hat{S}_{2i}\cdot\hat{S}_{2i+1}] \qquad (1)$$

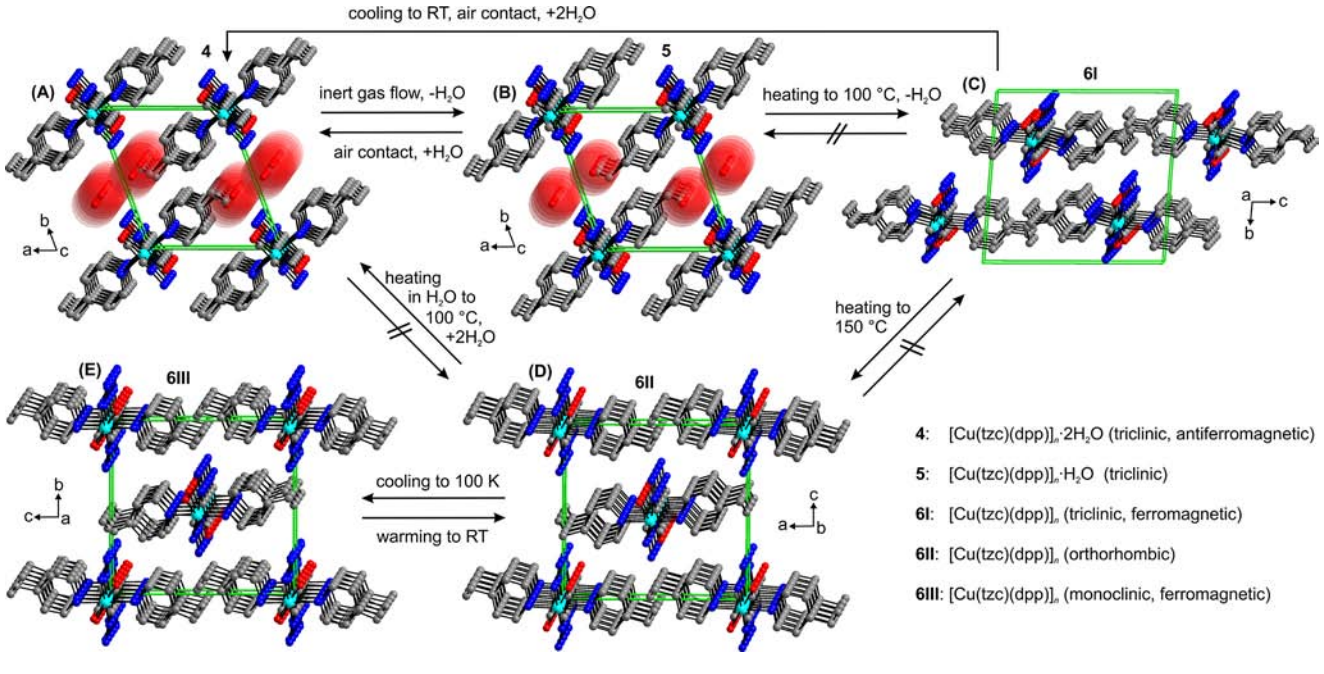

**Figure 11.** Crystal structures of the hydrates [Cu(tzc)(dpp)]$_n$·2H$_2$O (**4**, A), [Cu(tzc)(dpp)]$_n$·H$_2$O (**5**, B) and its polymorphic anhydrate modifications [Cu(tzc)(dpp)]$_n$ (**6I**, C; **6II**, D; **6III**, E) viewed as stacked chains in a single unit cell. Arrows and labels indicate the directions and conditions, respectively, for phase transitions occurring between these phases.

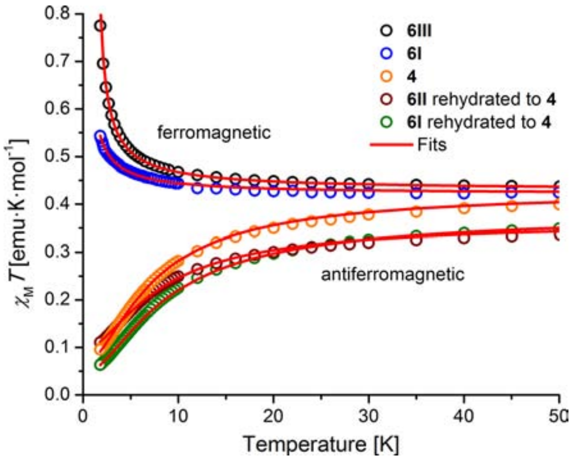

**Figure 12.** Low-temperature region (50−1.8 K) of the $\chi_M T$ temperature-dependence for all bulk materials presented in this manuscript. The red lines correspond to the best fit of magnetic chain models with $S = 1/2$. Full data up to $T = 300$ K are provided in the Figure S15.

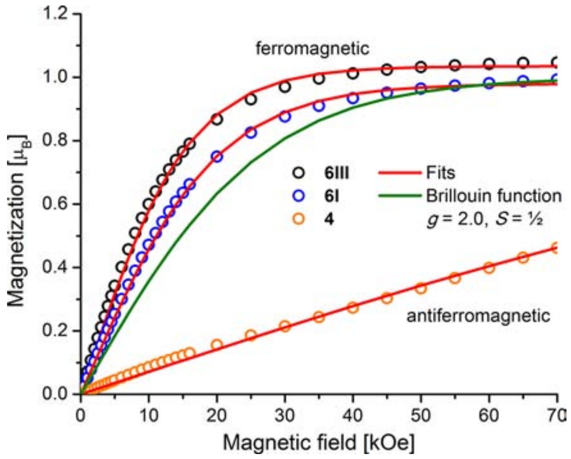

**Figure 13.** Isothermal field-dependent magnetizations for **4** (orange), **6I** (blue), and **6III** (black) at 1.8 K. The red lines represent the best fitting by a modified $S = 1/2$ Brillouin function. The green line represents the calculated curve for one isolated Cu(II) ion with $g = 2.0$ and $S = 1/2$ for comparison sake.

### Table 2. Fitting Parameters for Magnetic Data According to the Curie−Weiss Law for Compounds 4, 6I, and 6II/III[a]

| compound | $C$ [emu·K·mol$^{-1}$] | $\theta$ [K] | $\mu_{eff}$ (exp) [$\mu_B$] | $\mu_{eff}$ (calc) [$\mu_B$] | fit area [K] |
|---|---|---|---|---|---|
| **4** | 0.44 | −4.0 | 1.87 | 1.73 | 20−300 |
| **6I** | 0.42 | 0.5 | 1.83 | 1.73 | 1.8−300 |
| **6II/III** | 0.43 | 0.8 | 1.85 | 1.73 | 20−300 |

[a] See Figures S6−S8 for the data plots.

### Table 3. Fitting Parameters for Magnetic Data According to Different Chain Models for Compounds 4, 6I, and 6II/III

| compound | fitting model | ref | $S$ | $J$ [cm$^{-1}$] | $\alpha$ | $g$ |
|---|---|---|---|---|---|---|
| **4** | 1D linear-chain | 14 | 1/2 | −3.00 | 1.00 | 2.09 |
| **6I** | 1D alternating-chain | 14 | 1/2 | 0.55 | 0.55 | 2.11 |
| **6II/III** | 1D linear-chain | 16 | 1/2 | 0.60 | – | 2.12 |

Using an $\alpha$ value of 1 reduces this equation to a regular 1D linear-chain model producing an excellent fit of the experimental data over the whole temperature range with best fit parameters of $J = -3.0$ cm$^{-1}$ and $g = 2.09$ (Figure 12 and Table 3). The negative $J$ value further confirms antiferromagnetic interactions. Furthermore, at 1.8 K in an applied field of up to 70 kOe, the field dependence of the magnetization $M(H)$ increases almost linearly, reaching 0.46 $\mu_B$ at 70 kOe, which is far from the expected value of 0.99 $\mu_B$ from the Brillouin function for a $S = 1/2$ system with $g = 2.0$. The antiferromagnetic interaction was estimated to be $\theta = -7.6$ K by fitting the $M(H)$ data by using a modified Brillouin function according to Miller et al.[15] This negative $\theta$ is consistent with the antiferromagnetic nature of the Cu(II)···Cu(II) exchange interactions through the tetrazolate ligand (Figure 13).

$[Cu(tzc)(dpp)]_n$ (**6I** and **6II/III**): Temperature-independent $\chi_M T$ values for the anhydrate modifications **6I** and **6II/III** were recorded in the range 300−50 K with values of 0.42 for **6I** and 0.43 emu·K·mol$^{-1}$ for **6II/III**, respectively at 300 K, corresponding to $\mu_{eff} = 1.83$ for **6I** and 1.85 $\mu_B$ for **6II/III**, which is close to the expected spin-only value as described above. Upon further cooling, starting at ~50 K, increasing $\chi_M T$ values are observed, indicating the presence of ferromagnetic exchange interactions between adjacent Cu(II) centers. The $\chi_M^{-1}$ vs $T$ curves (Figures S7 and S8) yield to Curie constants of $C = 0.42$ for **6I** and 0.43 cm$^3$·K·mol$^{-1}$ for **6II/III** and positive Weiss constants of $\theta = +0.5$ for **6I** and +0.8 K for **6II/III**, which confirm the global ferromagnetic behavior (Table 2).

The crystal structures of the anhydrate modifications **6I** and **6II/III** provide different magnetic exchange pathways than those discussed above for the dihydrate **4**. Whereas in **4** the bridging tzc ligands are nearly symmetrical, in **6I** and **6II/III** this alignment is strongly distorted leading to different distances for the Cu−N$_{tzc}$ coordination. Moreover, in the crystal structure of **6I** two crystallographic independent Cu(II) cations are present, which enables two different magnetic exchange pathways to be operative (Figure 14). Taking these considerations into account, the magnetic data for **6I** were fit using the same Heisenberg exchange model as described above (Figure 12)[14] but with $\alpha$ as a refinable parameter. The result is a 1D alternating-chain model with best-fit parameters of $J = +0.55$ cm$^{-1}$, $g = 2.11$, and $\alpha = 0.55$ (Table 3), where $J$ is the exchange interaction between the two nearest-neighbor Cu(II) centers and $\alpha J$ is the exchange interaction between the two farthest-neighbor Cu(II) centers (Figure 14). According to the crystal structure of **6II/III**, two crystallographic related Cu(II) centers enable only one magnetic exchange pathway. Thus, the magnetic data for **6II/III** were fit by using a 1D linear-chain Heisenberg exchange model by Baker et al. for $S = 1/2$ systems with the Hamiltonian written as[16]

$$H = -J\sum_{i=1}^{n-1} S_{A_i}\cdot S_{A_{i+1}} \qquad (2)$$

Excellent fitting parameters of $J = +0.60$ cm$^{-1}$ and $g = 2.12$ were obtained (Figure 12 and Table 3). The positive $J$ values of **6I** and **6II/III** support the presence of ferromagnetic interactions. Moreover, $M(H)$ at 1.8 K show a steep increase in the magnetization data upon increasing the applied field, yielding saturated magnetization values of 0.98 $\mu_B$ for **6I** and 1.05 $\mu_B$ for **6II/III** at 70 kOe in good agreement with the expected value of 0.99 $\mu_B$. Fitting of the $M(H)$ data by a Brillouin function led to positive $\theta$ values of +0.5 K for **6I** and +0.7 K for **6II/6III**. This is a typical ferromagnetic behavior (Figure 13). Further susceptibility measurements of samples **6I** and **6II/III** rehydrated to the dihydrate **4** reveal that the change in their magnetic properties can be reversibly cycled with hydration and dehydration processes (Figure 12).

A recent study has shown that the Cu−N−C angles of imidazolyl bridging moieties significantly affect the magnitude of the magnetic exchange coupling.[17] According to their DFT calculations on a model consisting of a symmetrical dinuclear $\mu_2$−N1−N4 tetrazolate (tetr) bridging Cu(II) complex with the Cu(II) $d_{x^2-y^2}$ magnetic orbitals directed toward the $N_{tetr}$ atoms, the authors found that the larger the Cu−$N_{tetr}$−$C_{tetr}$ angle (115−140°), the stronger the antiferromagnetic interaction (e.g., $-1.1$ cm$^{-1}$ at 120° and $-17.6$ cm$^{-1}$ at 140°). Furthermore, they predicted that, in the range of 105−115°, even weakly ferromagnetic interactions (<+1 cm$^{-1}$) can occur. However, this latter prediction was not confirmed by experimental results. Hence, angles for **6I−III** in the range of 106−114° (Table 1) with $J$ = +0.55 and +0.60 cm$^{-1}$ (Table 3) confirm their calculations. In **4**, an angle slightly above 115° is observed, leading to $J = -3.00$ cm$^{-1}$, which is in reasonably good agreement with the aforementioned antiferromagnetic range. It should be noted that exact matching of $J$ values cannot be expected, because other structural factors, such as distortions of the equatorial Cu(II) coordination plane and Cu−Cu distances, can also affect the strength of the antiferromagnetic coupling. Thus, the theoretical $J$ dependence of the Cu−$N_{tetr}$−$C_{tetr}$ angle is only a qualitative trend with relatively accurate predictive values.[17] However, this model is a reasonable explanation of the dramatic change in the magnetic properties from antiferromagnetic interactions in the dihydrate **4** to weak ferromagnetic interactions in the anhydrate modifications **6I−III**.

Only very few polymeric coordination materials that exhibit reversible ferromagnetic ↔ antiferromagnetic ground-state transformations upon desolvation ↔ solvation processes have been described in the literature. Kurmoo et al. reported the porous framework $[Co_3(OH)_2(C_4O_4)_2]_n \cdot 3H_2O$ which reversibly exhibits ferromagnetic to antiferromagnetic properties upon dehydration−hydration.[8a] They found that the transformation is caused by the presence of antiferromagnetic coupling between the ferromagnetic framework *via* hydrogen-bonded water molecules in the pores rather than from a significant change in exchange coupling within the framework lattice. Lopez et al. described that the porous framework $[Mn_2(TCNQF_4)(CH_3OH)_{7.5}(H_2O)_{0.5}]_n \cdot 2TCNQF_4 \cdot 7.5CH_3OH$ reversibly transforms from glassy ferromagnetic to antiferromagnetic properties upon desolvation−solvation.[8c] These properties are attributed to the loss of coordinated methanol molecules with subsequent structural rearrangement and binding of uncoordinated $[TCNQF4]^{-\bullet}$ radicals to the Mn(II) ions which results in stronger magnetic communication, as observed for the solvated material. Cheng et al. described that the porous framework $[KCo_7(OH)_3(\text{isophthalate})_6(H_2O)_4]_n \cdot 12H_2O$ reversibly displays antiferromagnetic vs superparamagnetic properties upon dehydration−hydration.[8f] These authors state that this transformation is caused by large geometric changes of the metal coordination environments due to loss of coordinated water molecules. Motokawa et al. demonstrated that the compound $[\{Ru_2(O_2CPh\text{-}o\text{-}Cl)_4\}2TCNQ(MeO)_2]_n \cdot CH_2Cl_2$ reversibly transforms from ferromagnetic to antiferromagnetic long-range ordering upon desolvation−solvation.[8g] They reported that this reversible magnetism is triggered by a subtle order/disorder of a ligand substituent due to the solvation/desolvation. The presented reported change of the magnetic properties from antiferromagnetic coupling in **4** to ferromagnetic coupling in **6I−III** reported herein is different from the above examples. The loss of uncoordinated interchain water molecules in **4** causes subtle reorientations of the tzc ligand in **6I−III** (Figure 14). This leads to a significant change in the exchange coupling within the framework, as described by the aforementioned DFT calculations.

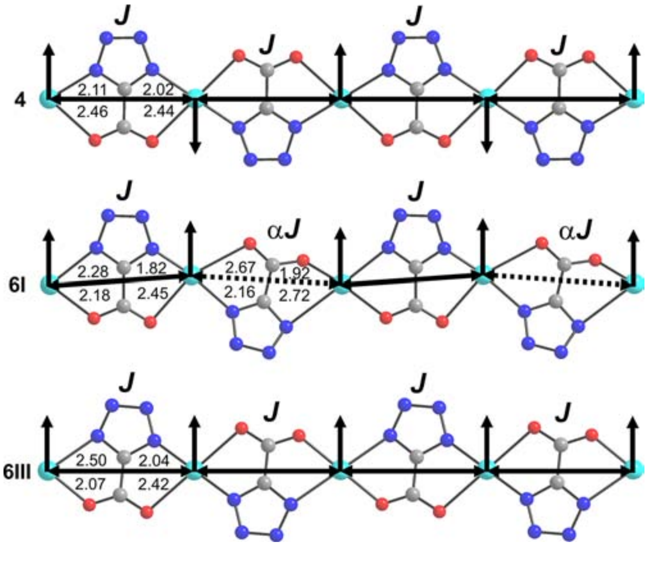

**Figure 14.** Schematic representation of the magnetic exchange pathways in **4** (top), **6I** (middle), and **6III** (bottom). The Cu−$N_{tzc}$/$O_{tzc}$ bond distances are given in Å.

## ■ CONCLUSIONS

In this contribution, eight new metal−organic magnetic materials based on copper(II) tetrazolate-5-carboxylate with 1,3-di(4-pyridyl)propane as a neutral N-donor spacer ligand have been synthesized and investigated for their structures, thermal reactivity, and magnetic properties. Surprisingly, a hydrothermal one-pot synthesis of $Cu(OAc)_2$, tzc, and dpp leads to the simultaneous formation of three different single-crystalline solvate materials **1−3**. This is a rare phenomenon that underscores the very close lattice enthalpies of these compounds. In a hydrothermal bulk synthesis process, none of them can be prepared as crystalline pure phases; instead a phase pure bulk material of the new dihydrate **4** is obtained. Systematic investigation of its thermal properties by temperature-dependent *in situ* synchrotron-based powder diffraction experiments has shown multiple phase transitions with temperature changes. The dihydrate **4** transforms *via* the monohydrate intermediate **5** into three different polymorphic anhydrate modifications **6I−III**, a trimorphic system. All crystal structures were determined by powder diffraction data and show the same framework topology with Cu(II) cations each coordinated by two bridging dpp and tzc ligands in an octahedral geometry forming $[Cu(tzc)(dpp)]_n$ 1D chains. In this case, the Cu(II)···Cu(II) bridging tzc ligand constitutes a good pathway to mediate interesting magnetic properties. Upon phase transitions, distinct differences in the orientation of the tzc ligand are observed leading to dramatic changes in the magnetic behavior: Whereas in the dihydrate **4**, antiferromagnetic interactions are present, the trimorphic anhydrate system exhibits ferromagnetic properties.

The switching between ferro- and antiferromagnetic coupling that accompanies structural phase transitions is unique for simple 1D magnetic MOFs. In addition, the high structural diversity of eight different 1D MOF materials with identical metal/ligand compositions is unprecedented. Switching between different magnetic states occurs due to subtle guest-induced structural changes. Notably, the anhydrate **6I**, which exhibits ferromagnetic coupling, is air unstable and transforms to the antiferromagnetic dihydrate **4** in contact with ambient laboratory atmosphere. On the other hand the anhydrate's **6II** ferromagnetic state is maintained in air.

The rational design of magnetic-switchable MOF materials requires fundamental knowledge of magneto−structural correlations. The structural information, however, is typically obtained from *ex situ* single crystal-to-single crystal transformation X-ray diffraction experiments, but such data are rarely available due to lack of single crystals. In the present study, we have shown that one can resolve these issues by using *in situ* synchrotron-based powder diffraction experiments. Clearly, more systematic studies on magneto−structural correlations of similar framework materials are needed to gain additional fundamental insight into such magnetic tunable systems. In this vein, the herein presented systematic experimental approach of combination thermoanalytic, infrared spectroscopic, and powder diffraction techniques will be part of future studies to investigate the influence of different paramagnetic transition-metal ions in similar tzc containing metal−organic magnetic materials.

## ■ EXPERIMENTAL SECTION

**General Information.** Commercially available reagents were used as received without further purification. The tetrazolate-5-carboxylate $(tzc)^{2-}$ ligand was produced *in situ* by hydrothermal treatment of the 1H-tetrazole-5-carboxylic acid ethyl ester sodium salt (NaEttzc). Caution! Although not encountered in our experiments, metal complexes of tetrazolate compounds are potentially explosive. Only a small amount of the materials should be prepared and handled with care.

**Synthesis of $[Cu(tzc)(dpp)]_n \cdot 0.5hexane \cdot 0.5H_2O$ (1), $[Cu(tzc)(dpp)]_n \cdot 4.5H_2O$ (2), and $[Cu(tzc)(dpp)]_n \cdot 1.25hexane$ (3).** Single crystals suitable for X-ray diffraction studies were isolated from the reaction of a mixture containing $Cu(OAc)_2$ (18.2 mg, 0.1 mmol), NaEttzc (16.4 mg, 0.1 mmol), dpp (19.8 mg, 0.1 mmol), and 3 mL of $H_2O$ at 100 °C after sitting for 4 days. Upon cooling, a mixture of light-purple rod-shaped single crystals of **1** and blue block-shaped single crystals of **2** and **3** were obtained. Bulk materials of these compounds could not be prepared; all attempts lead to the formation of **4**.

**Synthesis of $[Cu(tzc)(dpp)]_n \cdot 2H_2O$ (4).** A microcrystalline bulk material was prepared by a reaction of $Cu(OAc)_2$ (181.6 mg, 1.0 mmol), NaEttzc (164.1 mg, 1.0 mmol), and dpp (198.2 mg, 1.0 mmol) in 15 mL $H_2O$. After stirring the mixture at 150 °C for 1 day, the resultant light-purple precipitate was filtered, washed with $H_2O$, EtOH, and $Et_2O$, and dried in air. Yield: 386.8 mg (94.4%). The purity was verified by XRPD (Figure S9). Elemental analysis for $C_{15}H_{18}CuN_6O_4$ (409.89), calcd (%): C, 43.95; H, 4.43; N, 20.50. Found (%): C, 44.06; H, 4.35; N, 20.59. IR: $\tilde{\nu}$ = 3663 (w), 3391 (br), 2963 (w), 1620 (vs), 1614 (vs), 1487 (m), 1443 (s), 1433 (s), 1335 (s), 1225 (m), 1209 (m), 1198 (w), 1130 (w), 1072 (m), 1040 (m), 1020 (w), 862 (w), 837 (m), 825 (m), 806 (s), 760 (w), 680 (s), 633 (w) $cm^{-1}$ (Figure S10).

**Synthesis of $[Cu(tzc)(dpp)]_n$ (6I).** Heating of **4** to 100 °C and holding this temperature for 30 min under a dynamic $N_2$ atmosphere leads to the formation of a light-purple polycrystalline sample of **6I**. This intermediate was transferred into a glovebox to prepare sample holders for magnetic and *ex situ* X-ray measurements. The phase purity of **6I** and its reversible retransformation to **4** upon air contact was determined from the X-ray data (Figure S11).

**Synthesis of $[Cu(tzc)(dpp)]_n$ (6II).** Heating of **4** to 150 °C and holding this temperature for 30 min in air leads to the formation of a gray polycrystalline sample of **6II**. No special treatment of **6II** for further investigations is needed due to its moisture and air stability. The purity was checked by XRPD (Figure S12). Elemental analysis for $C_{15}H_{14}CuN_6O_2$ (373.86), calcd (%): C, 48.19; H, 3.77; N, 22.48. Found (%): C, 48.17; H, 3.74; N, 22.44. IR: $\tilde{\nu}$ = 3059 (w), 2926 (w), 2876 (w), 1950 (w), 1602 (vs), 1506 (w), 1483 (m), 1427 (m), 1323 (s), 1223 (w), 1179 (w), 1125 (m), 1080 (m), 1038 (m), 1028 (m), 955 (w), 866 (w), 833 (s), 800 (m), 764 (m), 741 (w), 683 (m), 669 (w) $cm^{-1}$ (Figure S13).

**Single-Crystal X-ray Diffraction Analysis.** Crystal data, details of data collection, and structural refinement parameters for compounds **1**−**3** are presented in Table 4. The X-ray diffraction experiments were carried out with a Bruker SMART APEX II diffractometer with a CCD area detector (graphite monochromatic Mo K$\alpha$ radiation, $\lambda$ = 0.71073 Å, $\omega$-scans with a 0.5° step in $\omega$). The semiempirical method SADABS[18] was applied for absorption correction. The structures were solved by direct methods and refined by the full-matrix least-squares technique against $|F|^2$ with the anisotropic temperature parameters for all nonhydrogen atoms. All H atoms were geometrically placed and refined in riding model approximation. Data reduction and further calculations were performed using the Bruker SAINT[19] and SHELXTL[20] program packages.

**Table 4. Selected Crystallographic Parameters and Refinement Details from Single Crystal Data for Compounds 1−3**

| compound | 1 | 2 | 3 |
|---|---|---|---|
| formula | $C_{18}H_{22}CuN_6O_{2.5}$ | $C_{15}H_{14}CuN_6O_2$ | $C_{15}H_{14}CuN_6O_2$ |
| MW [$g \cdot mol^{-1}$] | 425.96 | 373.86 | 373.86 |
| crystal system | triclinic | monoclinic | monoclinic |
| space group | $P\bar{1}$ | $C2/c$ | $C2/c$ |
| $a$ [Å] | 8.966(3) | 19.529(9) | 21.663(7) |
| $b$ [Å] | 10.032(4) | 10.884(4) | 23.202(7) |
| $c$ [Å] | 11.215(4) | 19.479(7) | 12.786(4) |
| $\alpha$ [°] | 74.336(5) | 90 | 90 |
| $\beta$ [°] | 72.466(5) | 108.276(7) | 113.847(6) |
| $\gamma$ [°] | 65.955(4) | 90 | 90 |
| $V$ [$Å^3$] | 865.8(6) | 3932(3) | 5878(3) |
| $T$ [K] | 120 | 110(2) | 110(2) |
| $Z$ | 2 | 8 | 12 |
| $D_{calc}$ [$g \cdot cm^{-3}$] | 1.634 | 1.263 | 1.267 |
| $\mu$ [$mm^{-1}$] | 1.293 | 1.128 | 1.132 |
| min/max transmission | 0.6126/0.9746 | 0.6611/0.8058 | 0.6015/0.7276 |
| $\theta_{max}$ [°] | 27.00 | 27.00 | 26.00 |
| measured reflections | 9736 | 21459 | 30395 |
| unique reflections | 3748 | 4265 | 5760 |
| reflections [$I > 2\sigma(I_0)$] | 2396 | 3292 | 3618 |
| parameters | 257 | 244 | 281 |
| $R_{int}$ | 0.0652 | 0.0591 | 0.0761 |
| $R_1$ [$I > 2\sigma(I_0)$] | 0.0589 | 0.0394 | 0.1121 |
| $wR_2$ [all data] | 0.1399 | 0.0871 | 0.2375 |
| GOF | 1.025 | 1.004 | 1.027 |
| $\Delta\rho_{max}/\Delta\rho_{min}$ [$e \cdot Å^{-3}$] | 1.00/−1.07 | 0.53/−0.34 | 1.87/−1.73 |

During the structure refinement of compound **2** and **3**, deviations from planarity as well as bond length and bond angle distortions were found in the tzc ligand. Several additional high residual peaks of electron density are located in the plane of the tzc, which are attributed to disorder of the tzc ligand. The disorder was modeled over two positions located in the same plane but with opposite head-to-tail orientations. It worth mentioning that in the case of compound **2**, such disorder is probably statistical, whereas in compound **3**, the tzc disorder occurs around a special position (a center of inversion).

Disorders were modeled successfully, and they were refined with the help of restrains on C−C, C−N, N−N, and C−O distances in tzc molecules and displacement parameters as well as rigid bond restraints for anisotropic displacement parameters. In the case of compound **2**,

Table 5. Selected Crystallographic Parameters and Refinement Details from Powder Data for Compounds 4−6III

| compound | 4 | 5 | 6I | 6II | 6III |
|---|---|---|---|---|---|
| formula | $C_{15}H_{18}CuN_6O_4$ | $C_{15}H_{16}CuN_6O_3$ | $C_{15}H_{14}CuN_6O_2$ | $C_{15}H_{14}CuN_6O_2$ | $C_{15}H_{14}CuN_6O_2$ |
| MW [g·mol$^{-1}$] | 409.89 | 391.88 | 373.86 | 373.86 | 373.86 |
| crystal system | triclinic | triclinic | triclinic | orthorhombic | monoclinic |
| space group | $P\bar{1}$ | $P\bar{1}$ | $P\bar{1}$ | *Pnma* | $P2_1/c$ |
| *a* [Å] | 9.0102(8) | 8.8876(6) | 11.3244(10) | 12.5434(3) | 11.1761(3) |
| *b* [Å] | 10.0302(9) | 9.8698(7) | 12.0673(12) | 11.2251(2) | 11.8084(4) |
| *c* [Å] | 11.2964(8) | 11.3149(6) | 12.6145(12) | 11.9059(3) | 12.5239(4) |
| *α* [°] | 73.969(6) | 75.320(5) | 94.319(5) | 90 | 90 |
| *β* [°] | 72.081(7) | 73.151(6) | 91.205(8) | 90 | 91.705(3) |
| *γ* [°] | 65.936(4) | 68.201(4) | 95.485(7) | 90 | 90 |
| *V* [Å$^3$] | 873.51(13) | 870.04(10) | 1710.4(3) | 1676.36(7) | 1652.07(9) |
| *T* [K] | 295 | 295 | 423 | 295 | 100 |
| *Z* | 2 | 2 | 4 | 4 | 4 |
| $D_{calc}$ [g·cm$^{-3}$] | 1.5426 | 1.4877 | 1.4514 | 1.4809 | 1.5026 |
| *μ* [mm$^{-1}$] | 0.859 | 0.831 | 0.841 | 0.308 | 0.312 |
| *λ* [Å] | 0.6124 | 0.60505 | 0.60505 | 0.41308 | 0.41308 |
| 2*θ* range [°] | 3.00−34.94 | 2.9−25.82 | 2.5−25.69 | 1.80−26.0 | 1.8−28.5 |
| no. parameters | 51 | 42 | 57 | 47 | 47 |
| $R_p$, $R_{wp}$ | 0.0443, 0.0585 | 0.0534, 0.0729 | 0.0492, 0.0646 | 0.0785, 0.0968 | 0.0813, 0.1015 |
| GOF | 3.45 | 1.830 | 1.610 | 1.220 | 1.220 |
| $R_{Bragg}$ | 0.0549 | 0.0515 | 0.0549 | 0.0533 | 0.0296 |

the relative occupancies for the disordered components were refined freely while constraining the total occupancy of all components to unity. As a result of refinement, relative occupancies of those two positions were found to be 75% and 25%. For compound **3**, the occupancy of the disordered tzc ligand was fixed to be 50%.

In the structures of compounds **2** and **3** there are large channels which are occupied by heavily disordered solvent molecules. Modeling attempts using a mixture of water and/or hexane were attempted, but no satisfactory disorder model could be achieved, and therefore the Squeeze program implemented in PLATON[21] was used to model this electron density. The program calculated a solvent-accessible volume of 1009.9 Å$^3$ (25.7% of the total unit cell volume) for compound **2** and 1545.2 Å$^3$ (26.3% of the total unit cell volume) for compound **3**, which were then removed from subsequent structure factor calculations.

CCDC-911805 (**1**), −911806 (**2**), −911807 (**3**), −911808 (**4**), −911809 (**5**), −911810 (**6I**), −911811 (**6II**), and −9118012 (**6III**) contain the supplementary crystallographic data for this paper. These data can be obtained free of charge from the Cambridge Crystallographic Data Centre *via* www.ccdc.cam.ac.uk.

**Structure Determination by Synchrotron-Based Powder Diffraction.** Powder X-ray diffraction data for compounds **4**, **5**, and **6I** were recorded *in situ* on 1-BM-C beamline using a flow-cell setup.[22] Patterns for compounds **6II** and **6III** were obtained *ex situ* on 11-BM-C beamline at the Advanced Photon Source in Argonne National Laboratory (Argonne, IL, U.S.A.) from samples contained in 0.9 mm diameter polyimide capillaries. The parameters of the data collection and final Rietveld refinements for these compounds are listed in Table 5. In the case of compounds **6I** and **6III** the temperatures of the samples were controlled *via* an Oxford Cryosystems Cryostream 700 Plus. Patterns for all compounds were indexed with the use of the TOPAS 4.2[23] software. To simplify structural determination, all samples were assumed to be centrosymmetric; systematic absences in the cases of **6II** and **6III** were consistent with the space groups *Pnma* and $P2_1/c$.

Structure solutions were performed with FOX[24] software using the parallel tempering technique. The structures of **4**−**6III** were finally refined using Jana2006. Twelve Legendre polynomials were used to adjust the background with a pseudo-Voigt function to determine the peak profile. One overall thermal parameter was also applied during refinements. Distance and angle constraints were used during the refinement to refine the ligands as a rigid body. The final Rietveld refinement plots and the agreement factors are satisfactory and can be seen in Figure S14 and Table 5, respectively.

**Thermogravimetric Analyses and Differential Scanning Calorimetry Coupled to Mass spectroscopy (TG-DSC-MS).** TG-DSC-MS data were recorded using a TGA/DSC 1 STAR system from Mettler Toledo, which is coupled to a mass spectrometer PrismaPlus QMG 220 M with a C-SEM-detector from Pfeiffer. All measurements were performed using $Al_2O_3$ crucibles in a dynamic argon atmosphere and a heating rate of 3 °C·min$^{-1}$. The instrument was corrected for buoyancy and current effects and was calibrated using standard reference materials.

**Elemental Analysis.** Elemental analyses (C, H, and N) were obtained by Atlantic Microlab, Inc.

**Spectroscopy.** FT-IR data were recorded on an IRAffinity-1 instrument from SHIMADZU.

**Magnetic Measurements.** Magnetic data were collected on crushed polycrystalline samples with the use of a Quantum Design SQUID magnetometer MPMS-XL. The dc magnetic susceptibility measurements were carried out in an applied field of 1000 Oe over the temperature range of 300−1.8 K. Magnetization data were measured at 1.8 K with the magnetic field varying from 0 to 70 kOe. The data were corrected for diamagnetic contributions calculated from the Pascal constants.[25] All magnetic measurements were performed on the same sample beginning as the dihydrate **4** phase, which was consecutively transformed upon heating to the anhydrate modifications **6I** and **6II** and finally rehydrated to **4** to show the reversibility of the magnetic sponge-like properties. These measurements were repeated twice with to different freshly synthesized sample batches.

## ■ ASSOCIATED CONTENT

### Supporting Information

Temperature ellipsoid structure plots and further structural information of **1**−**3**; experimental and calculated XRPD patterns of **4**, **6I** and **6II**; IR spectroscopic data of **4** and **6II**; $\chi_M^{-1}$ vs *T* plots including Curie−Weiss fits of **4**, **6I**−**III**; $\chi_M T$ vs *T* plot up to 300 K of **4** and **6I**−**III**, *in situ* SPD pattern of **6II** upon cooling to 100 K; final Rietveld refinement profiles for compounds **4**−**6III**. This information is available free of charge via the Internet at http://pubs.acs.org.

## ■ AUTHOR INFORMATION

### Corresponding Author

zhou@chem.tamu.edu

## Notes

The authors declare no competing financial interest.

## ■ ACKNOWLEDGMENTS

Funding was provided by U.S. Department of Energy (DE-SC0001015 and DE-FC36-07GO17033) and the Welch Foundation (A-1725). Dr. Mario Wriedt thanks the Postdoc Program of the German Academic Exchange Service (DAAD) for his financial support. Use of the Advanced Photon Source, an Office of Science User Facility operated for the U.S. Department of Energy (DOE) Office of Science by Argonne National Laboratory, was supported by the U.S. DOE under contract no. DE-AC02-06CH11357. We thank Prof. Karen Wooley for access to her experimental facilities and Mr. Kevin Pollack for his support in the TG-DSC-MS measurements. Special thanks to Prof. Christian Näther from the University of Kiel for useful discussions. The magnetic measurements were conducted in the Department of Chemistry SQUID Facility with a magnetometer obtained by a grant from the National Science Foundation (CHE-9974899). Prof. Dunbar thanks the DOE (DE-FG02-02ER45999) for support of Dr. Andrey Prosvirin. A detailed description is provided in the SI.

## ■ REFERENCES

(1) (a) Wang, C.; Tao, S.; Wei, W.; Meng, C.; Liu, F.; Han, M. *J. Mater. Chem.* **2010**, *20*, 4635. (b) Corma, A.; Diaz, U.; Garcia, T.; Sastre, G.; Velty, A. *J. Am. Chem. Soc.* **2010**, *132*, 15011. (c) Nunes, J.; Herlihy, K. P.; Mair, L.; Superfine, R.; DeSimone, J. M. *Nano Lett.* **2010**, *10*, 1113. (d) Nayak, S.; Malik, S.; Indris, S.; Reedijk, J.; Powell, A. K. *Chem.—Eur. J.* **2010**, *16*, 1158. (e) Rolison, D. R.; Long, J. W.; Lytle, J. C.; Fischer, A. E.; Rhodes, C. P.; McEvoy, T. M.; Bourg, M. E.; Lubers, A. M. *Chem. Soc. Rev.* **2009**, *38*, 226.

(2) (a) Czaja, A. U.; Trukhan, N.; Muller, U. *Chem. Soc. Rev.* **2009**, *38*, 1284. (b) Lee, J.; Farha, O. K.; Roberts, J.; Scheidt, K. A.; Nguyen, S. T.; Hupp, J. T. *Chem. Soc. Rev.* **2009**, *38*, 1450. (c) Li, J. R.; Kuppler, R. J.; Zhou, H. C. *Chem. Soc. Rev.* **2009**, *38*, 1477. (d) Murray, L. J.; Dinca, M.; Long, J. R. *Chem. Soc. Rev.* **2009**, *38*, 1294. (e) Yaghi, O. M.; O'Keeffe, M.; Ockwig, N. W.; Chae, H. K.; Eddaoudi, M.; Kim, J. *Nature* **2003**, *423*, 705. (f) Allendorf, M. D.; Bauer, C. A.; Bhakta, R. K.; Houk, R. J. T. *Chem. Soc. Rev.* **2009**, *38*, 1330. (g) Kuppler, R. J.; Timmons, D. J.; Fang, Q. R.; Li, J. R.; Makal, T. A.; Young, M. D.; Yuan, D. Q.; Zhao, D.; Zhuang, W. J.; Zhou, H. C. *Coord. Chem. Rev.* **2009**, *253*, 3042. (h) Wriedt, M.; Näther, C. *Z. Anorg. Allg. Chem.* **2009**, *635*, 2459.

(3) (a) Blake, A. J.; Champness, N. R.; Hubberstey, P.; Li, W.-S.; Withersby, M. A.; Schröder, M. *Coord. Chem. Rev.* **1999**, *183*, 117. (b) Brammer, L. *Chem. Soc. Rev.* **2004**, *33*, 476. (c) Desiraju, G. R. *Angew. Chem., Int. Ed.* **2007**, *46*, 8342. (d) Miller, J. S. *CrystEngComm* **2005**, *7*, 458. (e) Boeckmann, J.; Wriedt, M.; Näther, C. *Eur. J. Inorg. Chem.* **2010**, 1820. (f) Wriedt, M.; Näther, C. *Dalton Trans.* **2011**, *40*, 886.

(4) (a) Janiak, C. *Dalton Trans.* **2003**, 2781. (b) Kurmoo, M. *Chem. Soc. Rev.* **2009**, *38*, 1353. (c) Maspoch, D.; Ruiz-Molina, D.; Veciana, J. *J. Mater. Chem.* **2004**, *14*, 2713. (d) Pardo, E.; Ruiz-Garcia, R.; Cano, J.; Ottenwaelder, X.; Lescouezec, R.; Journaux, Y.; Lloret, F.; Julve, M. *Dalton Trans.* **2008**, 2780. (e) Rao, C. N. R.; Cheetham, A. K.; Thirumurugan, A. *J. Phys.: Condens. Matter* **2008**, *20*, 083202. (f) Miller, J. S. *Dalton Trans.* **2006**, 2742. (g) Dechambenoit, P.; Long, J. R. *Chem. Soc. Rev.* **2011**, *40*, 3249.

(5) (a) Kitagawa, S.; Kitaura, R.; Noro, S. *Angew. Chem., Int. Ed.* **2004**, *43*, 2334. (b) Kitagawa, S.; Uemura, K. *Chem. Soc. Rev.* **2005**, *34*, 109. (c) Férey, G.; Serre, C. *Chem. Soc. Rev.* **2009**, *38*, 1380. (d) Coronado, E.; Giménez-López, M. C.; Korzeniak, T.; Levchenko, G.; Romero, F. M.; Segura, A.; García-Baonza, V. n.; Cezar, J. C.; de Groot, F. M. F.; Milner, A.; Paz-Pasternak, M. *J. Am. Chem. Soc.* **2008**, *130*, 15519.

(6) (a) Kaneko, W.; Ohba, M.; Kitagawa, S. *J. Am. Chem. Soc.* **2007**, *129*, 13706. (b) Milon, J.; Daniel, M. C.; Kaiba, A.; Guionneau, P.; Brandes, S.; Sutter, J. P. *J. Am. Chem. Soc.* **2007**, *129*, 13872. (c) Navarro, J. A. R.; Barea, E.; Rodriguez-Dieguez, A.; Salas, J. M.; Ania, C. O.; Parra, J. B.; Masciocchi, N.; Galli, S.; Sironi, A. *J. Am. Chem. Soc.* **2008**, *130*, 3978. (d) Sun, W. W.; Tian, C. Y.; Jing, X. H.; Wang, Y. Q.; Gao, E. Q. *Chem. Commun.* **2009**, 4741. (e) Wang, Z. M.; Zhang, B.; Fujiwara, H.; Kobayashi, H.; Kurmoo, M. *Chem. Commun.* **2004**, 416.

(7) (a) Halder, G. J.; Kepert, C. J.; Moubaraki, B.; Murray, K. S.; Cashion, J. D. *Science* **2002**, *298*, 1762. (b) Neville, S. M.; Halder, G. J.; Chapman, K. W.; Duriska, M. B.; Southon, P. D.; Cashion, J. D.; Letard, J. F.; Moubaraki, B.; Murray, K. S.; Kepert, C. J. *J. Am. Chem. Soc.* **2008**, *130*, 2869.

(8) (a) Kurmoo, M.; Kumagai, H.; Chapman, K. W.; Kepert, C. J. *Chem. Commun.* **2005**, 3012. (b) Kahn, O.; Larionova, J.; Yakhmi, J. V. *Chem.—Eur. J.* **1999**, *5*, 3443. (c) Lopez, N.; Zhao, H. H.; Prosvirin, A. V.; Chouai, A.; Shatruk, M.; Dunbar, K. R. *Chem. Commun.* **2007**, 4611. (d) Maspoch, D.; Ruiz-Molina, D.; Wurst, K.; Domingo, N.; Cavallini, M.; Biscarini, F.; Tejada, J.; Rovira, C.; Veciana, J. *Nat. Mater.* **2003**, *2*, 190. (e) Zhang, X. M.; Hao, Z. M.; Zhang, W. X.; Chen, X. M. *Angew. Chem., Int. Ed.* **2007**, *46*, 3456. (f) Cheng, X. N.; Zhang, W. X.; Lin, Y. Y.; Zheng, Y. Z.; Chen, X. M. *Adv. Mater.* **2007**, *19*, 1494. (g) Motokawa, N.; Matsunaga, S.; Takaishi, S.; Miyasaka, H.; Yamashita, M.; Dunbar, K. R. *J. Am. Chem. Soc.* **2010**, *132*, 11943.

(9) Wriedt, M.; Zhou, H.-C. *Dalton Trans.* **2012**, *41*, 4207.

(10) (a) Jia, Q.-X.; Tian, H.; Yan, L.; Ma, Y.; Gao, E.-Q. *Inorg. Chim. Acta* **2010**, *363*, 3750. (b) Jia, Q.-X.; Sun, W.-W.; Yao, C.-F.; Wu, H.-H.; Gao, E.-Q.; Liu, C.-M. *Dalton Trans.* **2009**, 2721. (c) Jia, Q.-X.; Wang, Y.-Q.; Yue, Q.; Wang, Q.-L.; Gao, E.-Q. *Chem. Commun.* **2008**, 4894. (d) Rodriguez-Dieguez, A.; Mota, A. J.; Cano, J.; Ruiz, J.; Choquesillo-Lazarte, D.; Colacio, E. *Dalton Trans.* **2009**, 6335.

(11) Wriedt, M.; Sculley, J. P.; Yakovenko, A. A.; Ma, Y.; Halder, G. J.; Balbuena, P. B.; Zhou, H.-C. *Angew. Chem., Int. Ed.* **2012**, *51*, 9804.

(12) Zeleňák, V.; Vargová, Z.; Györyová, K. *Spectrochim. Acta* **2007**, *A66*, 262.

(13) Bernstein, J.; Davey, R. J.; Henck, J.-O. *Angew. Chem., Int. Ed.* **1999**, *38*, 3440.

(14) Hall, J. W.; Marsh, W. E.; Weller, R. R.; Hatfield, W. E. *Inorg. Chem.* **1981**, *20*, 1033.

(15) Shum, W. W.; Liao, Y.; Miller, J. S. *J. Phys. Chem. A* **2004**, *108*, 7460.

(16) Baker, G. A., Jr.; Rushbrooke, G. S.; Gilbert, H. E. *Phys. Rev.* **1964**, *135*, A1272.

(17) Mota, A. J.; Rodríguez-Diéguez, A.; Palacios, M. A.; Herrera, J. M.; Luneau, D.; Colacio, E. *Inorg. Chem.* **2010**, *49*, 8986.

(18) Sheldrick, G. M. *SADABS-2008/1, Absorption Correction Program*; Bruker AXS: Madison, Wisconsin, 2008.

(19) *SAINTPlus, Data Reduction and Correction Program v. 6.2*; Bruker AXS: Madison, Wisconsin, 2001.

(20) Sheldrick, G. M. *Acta Crystallogr.* **2008**, *A64*, 112.

(21) Spek, A. L. *PLATON, a Multipurpose Crystallographic Tool*; Utrecht University: Utrecht, The Netherlands, 2005.

(22) Chupas, P. J.; Chapman, K. W.; Kurtz, C.; Hanson, J. C.; Lee, P. L.; Grey, C. P. *J. Appl. Phys.* **2008**, *41*, 822.

(23) Young, R. A. *The Rietveld Method 1−39*; Oxford University Press: Oxford, U.K., 1993.

(24) Favre-Nicolin, V.; Cerny, R. *J. Appl. Crystallogr.* **2002**, *35*, 734.

(25) Bain, G. A.; Berry, J. F. *J. Chem. Educ.* **2008**, *85*, 532.